# Voltage Control of Antiferromagnetic Phases at Near-Terahertz Frequencies

Anthony Barra, John Domann, Ki Wook Kim, and Greg Carman

Phys. Rev. Applied **9**, 034017 — Published 21 March 2018

DOI: 10.1103/PhysRevApplied.9.034017

# Near THz Voltage Control Of Antiferromagnetic Phases

Anthony Barra[1], John Domann[1], Ki Wook Kim[2,3], Greg Carman[1]

[1] Department of Mechanical and Aerospace Engineering, University of California, Los Angeles, California, 90095, USA

[2] Department of Electrical and Computer Engineering, North Carolina State University, Raleigh, North Carolina, 27695, USA

[3] Department of Physics, North Carolina State University, Raleigh, North Carolina, 27695, USA

A method to control antiferromagnetism using voltage-induced strain was proposed and theoretically examined. Voltage-induced magnetoelastic anisotropy was shown to provide sufficient torque to switch an antiferromagnetic domain 90°, either from out-of-plane to in-plane, or between in-plane axes. Numerical results indicate that strain-mediated antiferromagnetic switching can occur in an 80 nm nanopatterned disk at frequencies approaching 1 THz, but that the switching speed heavily depends on the system's mechanical design. Furthermore, the energy cost to induce magnetic switching was only 450 aJ, indicating that magnetoelastic control of antiferromagnetism is substantially more energy efficient than other approaches.

There is a need to energy efficiently control magnetism at THz frequencies. Consequently, significant effort has been directed at controlling nanoscale magnetism by strain-coupling the magnetic and electric order parameters of composites containing piezoelectric and magnetoelastic materials. Such systems are highly energy efficient, with a predicted ~10 aJ/state switch [1-2], but have a frequency response limited by the magnetoelastic film's ferromagnetic resonance (usually ~1-10 GHz). Antiferromagnetic materials are attractive alternatives, because they exhibit resonances 2-3 orders of magnitude higher (~1 THz) [3-4], however, they are difficult to manipulate with external fields because the applied field needs to overcome the exchange anisotropy and induce a spin flop transition (which usually occurs for >1 Tesla). This paper proposes solving the 1 Tesla control problem by leveraging magnetoelastic coupling found in antiferromagnets like NiO [5-6], [36-39] or FeMn [7]. In particular, the uniaxial nature of the strain anisotropy enables rotation of the antiferromagnet phase without overcoming the antiferromagnetic exchange, and this lowers the required switching anisotropy by a factor of 10-100 times. To further analyze dynamics in such systems, we present a numerical framework which solves the 10 coupled partial differential equations that govern spatiotemporal magnetoelastic response in antiferromagnet-piezoelectric composites, and demonstrate energy efficient, ultra-fast switching. This strain-mediated voltage control of magnetism offers a new pathway to drive dynamic processes, on-chip, within the THz bandgap between radio and optical frequencies for the first time. This advancement may enable a new generation of strain-coupled antiferromagnetic sensors, spin wave devices, and systems with tunable exchange-biasing. Our findings also provide a clear direction for future research efforts to find magnetoelastic antiferromagnets with low intrinsic anisotropy.

Previous modeling efforts focused on predicting magnetoelastic dynamics in ferromagnets [8-10]. These models accounted for spatial non-uniformities in both strain and magnetization, thereby providing predictions that agreed with experimental data more closely than single-spin Stoner-Wohlfarth models or micromagnetic Landau-Lifshitz-Gilbert (LLG) models that assume uniform strain (i.e. mechanically decoupled models). Magnetoelastic models have been used to analyze voltage-controlled 180˚ switching in magnetic nanoelements with perpendicular magnetic anisotropy [11], in-plane magnetic switching driven by selective piezostraining using patterned electrodes [12-13], and 360˚ control of domain wall rotation in nickel ring structures [14] to name a few [15]. However, dynamic magnetoelastic models of

antiferromagnets have received little attention, and most antiferromagnetic models focus only on the micromagnetic behavior rather than mechanical coupling effects [16-17]. In particular, micromagnetic modeling has been used to predict the behavior of exchange-biased multilayers, specifically using finite elements [18] and the Monte Carlo method [19-20]. In experimental work, only magnetoelectricity in single phase materials [21-23] and carrier-induced spin reorientation [24-25] have previously been used for antiferromagnetic domain control. In this Letter, continuum-level numerical modeling illustrates that magnetoelasticity can provide a high speed, low power alternative control method for microscale antiferromagnets.

## I. Model Development

In this section, we provide the equations governing the spatiotemporal evolution of an antiferromagnetic material in response to voltage-induced strain. This formalism assumes that any antiferromagnetic phase can be deconstructed into two constituent ferromagnetic sublattices which are antiferromagnetically exchange coupled and oppositely oriented in the absence of external stimuli. Each of these sublattices is further assumed to be locally magnetically saturated throughout the entire volume. The sublattice magnetic moments are described by the vector field components $m_i^{(s)}(t)$, where i = {1,2,3} indicates the direction in a Cartesian coordinate system, and $s$ = {1, 2} indicates the sublattice. The model also assumes magneto- and electrostatics, infinitesimal strains, and neglects thermal influences.

Under these conditions, the dynamics of each magnetic sublattice follow the LLG equation [26],

$$\frac{\partial \underline{m}^{(s)}}{\partial t} = -\gamma \underline{m}^{(s)} \times \underline{H}_{eff} - \alpha \underline{m}^{(s)} \times \frac{\partial \underline{m}^{(s)}}{dt} \tag{1}$$

Where $\gamma$ is the gyromagnetic ratio, $\underline{H}_{eff}$ is the effective magnetic field, $\underline{m}^{(l)}$ is the sublattice magnetization direction, and $\alpha$ is the Gilbert damping parameter. $\underline{H}_{eff}$ is the driving term of the magnetic dynamics in Equation 1. It can vary in space and time, and is determined by taking the functional derivative of the total free energy density $E_{total}$

$$\underline{H}_{eff}^{(s)} = \frac{-1}{\mu_0 M_s} \frac{\partial E_{total}}{\partial \underline{m}^{(s)}} \tag{2}$$

where $\mu_0$ is the vacuum permeability and $M_s$ is the saturation magnetization. Equation 2 indicates that $\underline{H}_{eff}$ will contain a term for each magnetic anisotropy energy that contributes to $E_{total}$. In antiferromagnets with negligible magnetocrystalline anisotropy the relevant energy densities are

$$E_{total} = E_{ex}^{(1)} + E_{ex}^{(2)} + E_{AFM}^{(1-2)} + E_{me}^{(1)} + E_{me}^{(2)} \tag{3}$$

where $E_{ex}$, $E_{AFM}$, and $E_{me}$ denote the intralattice ferromagnetic exchange, the interlattice antiferromagnetic exchange, and magnetoelastic energy densities, respectively. This formulation of the energy densities assumes that all anisotropies besides those listed in Equation 3 are low relative to the strain-induced anisotropy. This assumption is reasonable as many magnetoelastic ferromagnets (Ni or FeGa), ferrimagnets (TbDyFe), and antiferromagnets (FeMn, MnNi, IrMn) [40-42] have low magnetocrystalline (MCA) or shape anisotropies relative to the strength of strain coupling. Including any of these smaller additional anisotropies like MCA or shape anisotropy would result in the formation of preferred axes of magnetic alignment (i.e. stable states), and modify the switching dynamics by creating energy wells which the strain-excitation must overcome. Since these changes may be complex, the model presented here addresses only amorphous antiferromagnets that are isotropic in-plane with stable states dictated by the exchange and magnetoelastic energies in Equation 3. The form of $E_{ex}$ used here is common in the literature $E_{ex}^{(s)} = A\nabla^2 \underline{m}^{(s)}$ [8][41], where $A$ is the exchange stiffness. The interlattice antiferromagnetic exchange is defined by an Ising-like term $E_{AFM}^{(1-2)} = -J\underline{m}^{(1)} \cdot \underline{m}^{(2)}$, where $J$ is the antiferromagnetic exchange coupling coefficient. In most antiferromagnets $J$ is sufficiently large that $-\underline{m}^{(1)} \approx \underline{m}^{(2)}$ [27], which cancels the dipolar fields and leads to zero demagnetization energy. The two remaining terms, $E_{me}^{(1)}$ and $E_{me}^{(2)}$, are functions of both strain and $\underline{m}^{(s)}$

$$E_{me}^{(s)} = \frac{1}{2}\left( \sum_i B_1 \varepsilon_{ii}^{total} (m_i^{(s)} m_i^{(s)} - \frac{1}{3}) + \sum_{i \neq j} B_2 \varepsilon_{ij}^{total} m_i^{(s)} m_j^{(s)} \right) \tag{4}$$

where $B_1$ and $B_2$ are the first and second order magnetoelastic coefficients.

Next, we present the effective fields used in the model, discuss the magnetomechanical coupling terms, and examine their connection to elastodynamic behavior. The two intralattice exchange fields are represented using the conventional ferromagnetic exchange term $H_{ex}^{(l)} = 2A(\mu_0 M_s)^{-1}\nabla^2 \underline{m}^{(l)}$ [28]. In contrast, the antiferromagnetic exchange field $H_{AFM}^{(s)}$ contains terms which allow the magnetization of one sublattice to influence the other. The i$^{th}$ component of these fields in each sublattice, respectively, are

$$\left[H_{AFM}^{(1)}\right]_i = -\frac{Jm_i^{(2)}}{\mu_0 M_s^{(1)}} \text{ and } \left[H_{AFM}^{(2)}\right]_i = -\frac{Jm_i^{(1)}}{\mu_0 M_s^{(2)}} \tag{5}$$

To simultaneously solve the coupled magnetoelastic dynamics, two additional coupling terms are needed. One of these terms, $H_{me}^{(l)}$, is an effective field that changes the sublattice magnetic state based on the total strain $\underline{\underline{\varepsilon}}^{total}$. The i$^{th}$ component of $H_{me}^{(l)}$ is

$$\left[H_{me}^{(s)}\right]_i = -\frac{1}{\mu_0 M_s^{(s)}}\left(B_1 \varepsilon_{ii}^{total} m_i^{(s)} + \sum_{j\neq i} B_2 \varepsilon_{ij}^{total} m_j^{(s)}\right) \tag{6}$$

where summation occurs only in the second term. This paper focuses on systems with isotropic magnetostriction, a condition which requires $\lambda_{100} = \lambda_{111} = \lambda_{110}$ and $B_1 = B_2$. Furthermore, the magnetostrictive coupling was assumed to affect each sublattice equally. This required 1) halving the magnitude of $\left[H_{me}^{(s)}\right]_i$ in equation 6 in comparison to the form for ferromagnets, and 2) defining $B_1^{Fe} = B_1^{Mn}$ and $B_2^{Fe} = B_2^{Mn}$. To maintain the self-consistency of the model, this reduction by half was also included in the magnetoelastic strain coupling term, $\underline{\underline{\varepsilon}}^{ME}$, which defines the strain caused by magnetic reorientation

$$\varepsilon_{ij}^{ME} = \frac{1}{2}\lambda_s\left(\frac{3}{2}\left[m_i^{(1)}m_j^{(1)} - \frac{1}{3}\right] + \frac{3}{2}\left[m_i^{(2)}m_j^{(2)} - \frac{1}{3}\right]\right) \tag{7}$$

where $\lambda_s$ is the saturation magnetostriction. In the limiting case of equation 7, when an antiferromagnet is uniformly magnetized, $\left|m_i^{(s)}m_j^{(s)}\right| \to 1$ and $\underline{\underline{\varepsilon}}^{ME} \to \lambda_s$ along the axis of

magnetization. This implies that saturation magnetostriction occurs when the two sublattices are coaxially aligned. Analogous behavior is observed in ferromagnets in the limit of magnetic saturation [26].

Equations 6-7 ensure that the mechanical and magnetic dynamics are coupled and can be solved simultaneously. However, calculation of $\underline{\underline{\varepsilon}}^{total}$ in equation 6 requires that the system's elastodynamics be considered. The governing equation of linear elastodynamics is

$$\rho \frac{\partial^2 \underline{u}}{\partial t^2} - \nabla \cdot \underline{\underline{\sigma}} = 0 \tag{8}$$

$$\underline{\underline{\sigma}} = \underline{\underline{\underline{\underline{C}}}} : \underline{\underline{\varepsilon}}^{mech} \tag{9}$$

where $\rho$ is the material density, $\underline{u}$ is the displacement, $\underline{\underline{\sigma}}$ is the elastic stress, $\underline{\underline{\underline{\underline{C}}}}$ is the stiffness, and $\underline{\underline{\varepsilon}}^{mech}$ is the elastic strain. The driving term in equation 9 is the mechanical strain $\underline{\underline{\varepsilon}}^{mech}$, which is the difference between the total strain $\underline{\underline{\varepsilon}}^{total}$ and the magnetic strain $\underline{\underline{\varepsilon}}^{ME}$. In this paper, we also consider cases where the antiferromagnet is externally strained by a piezoelectric material, in which case $\underline{\underline{\varepsilon}}^{mech}$ becomes

$$\underline{\underline{\varepsilon}}^{mech} = \underline{\underline{\varepsilon}}^{total} - \underline{\underline{\varepsilon}}^{piezo} - \underline{\underline{\varepsilon}}^{ME} \tag{10}$$

where $\underline{\underline{\varepsilon}}^{piezo}$ is the piezostrain. The strains in equation 10 are directly related to the physical displacements through $\underline{\underline{\varepsilon}}^{total} = \frac{1}{2}\left(\nabla \underline{u} + (\nabla \underline{u})^T\right)$.

Equations 2-7 and 9-10 were inserted into equations 1 and 8, resulting in nine coupled partial differential equations that govern antiferromagnetic magnetoelastic dynamics. In the case where piezoelectricity was included, one more differential equation was added to calculate the electric field distribution inside the piezoelectric layer. The coupled PDEs were solved simultaneously using a weighted residuals method within a finite element framework. The finite element solver used implicit time stepping ($t_{step}^{(\max)} = 0.5$ ps) and a backward differentiation

formula. In the antiferromagnetic volume, a cuboidal finite element mesh was used, with a maximum element size of 2.5 x 2.5 x 0.57 $nm^3$. This element size was chosen to capture any magnetic non-uniformities within the antiferromagnet's constituent ferromagnetic sublattices on the order of the exchange length, $L_{ex} = (2A_{ex})/(\mu_0 M_s^2)^{1/2} \approx 3.51$ nm, while simultaneously capturing any strain variations due to effects like shear lag.

The model developed above was used to study the two cases shown in Figures 1(a)-(b). In the first case (Figure 1(a)), an antiferromagnetic disk with an 80 nm radius and 4 nm thickness was modeled with traction free boundary conditions ($\underline{t} = \underline{\underline{\sigma}} \cdot \underline{n} = 0$) imposed at every surface. First, the disk's antiferromagnetic state was initialized out-of-plane (along $\hat{e}_3$) and relaxed for 50 ps. Then, at t=0, a uniform strain field was applied everywhere in the volume, with 1000 με of tension along $\hat{e}_2$ and 400 με of compression along $\hat{e}_1$. The average sublattice magnetic response was then recorded every 0.5 ps. Fourier analysis of the sublattice response to the broadband excitation allowed for identification of the antiferromagnetic resonance frequency.

In the second model (Figure 1(b)), an antiferromagnetic disk was attached to a thin piezoelectric film which, in turn, was attached to a thick substrate. The 400 x 400 x 100 $nm^3$ piezoelectric film was modeled with a mechanically clamped bottom surface ($\underline{u} = 0$) and fixed in-plane boundaries ($\underline{u} \cdot \hat{n} = 0$) to replicate the presence of the thick substrate and infinite extension of the film in the $\hat{e}_1$-$\hat{e}_2$ plane. The top surface of the composite was maintained traction free. As in the previous model, the disk's antiferromagnetic state was first initialized out-of-plane and relaxed for 50 ps. After relaxation, electrical ground (V = 0) was applied to the piezoelectric layer's bottom surface, while a voltage excitation, applied at either of the two 40 x 40 nm surface electrodes, was ramped from 0 to -0.5 V over 1.5 ps (see Figure 2(b) inset). The resulting piezostrain drove magnetic precession in the disk, which was recorded every 0.5 ps. As with the previous model, these boundary conditions were chosen because they lead to high but realistic strains, like those required for switching in other magnetoelastic materials.

The material properties used for both studies were as follows (bulk values were used where values for microscale geometries were not available, as they are known to be similar [34-36]). Since the material properties of magnetostrictive antiferromagnets are not well-studied, the

following constants were obtained from the available literature, using known constants for the ferromagnetic sublattices where relevant: $A_{ex\ (Fe)} \approx A_{ex\ (Mn)} = 2.48 \times 10^{-12}$ J/m [29], $M_{s\ (Fe)} \approx M_{s\ (Mn)} = 5.66 \times 10^5$ A/m, $\lambda_s \approx 750$ με [7], [30], Young's modulus $E = 77$ GPa [31], $\rho = 7700$ kg/m$^3$, and Poisson's ratio $\upsilon = 0.3$. A Gilbert damping parameter of $\alpha = 0.02$ was assigned to each ferromagnetic sublattice since this value is in the typical range for magnetoelastic ferromagnets [1, 42-43]. With these constants, the material modeled has a likeness to $Fe_{50}Mn_{50}$, whose antiferromagnetic exchange coupling coefficient, $J_{AFM}$, is currently unmeasured. Consequently, the value of the ferromagnetic exchange coefficient of bulk single crystal Fe, $J = 3.97 \times 10^6$ J/m$^3$, was used. In addition, a parametric sweep of α between 0.8 and 0.02 was used to confirm that value used for the Gilbert damping parameter did not significantly influence the threshold strain required for switching for realistic values of α (< 0.1). However, non-physical, high α values (> 0.7) produced a strongly overdamped response that changed the antiferromagnet's mechanical impedence and reduced strain transfer across the composite interface. For this reason, low α was used. With the material parameters used above, the magnetic and magnetostrictive predictions of the model cannot be quantitatively accurate for a particular material, but are intended to represent correct trends in the material behavior and exemplify proper modeling methods. The piezoelectric layer's properties were those of transversely isotropic $Pb[Zr_xTi_{1-x}]O_3$ (PZT). These were $d_{13}$ = -6.62 C/m$^2$, $d_{33}$ = 23.24 C/m$^2$, $\rho = 7500$ kg/m$^3$, $E_1$ = 127 GPa, $E_2$ = 82 GPa, $G_{13}$ = 22.9 GPa, $\varepsilon_{11} = \varepsilon_{22} = 3130$, and $\varepsilon_{33} = 3400$.

## II. Results and Discussion

Figure 2(a) shows the results for the model geometry illustrated in Figure 1(a) after uniform strain was applied at t=0 ps. The components of the Fe sublattice magnetization, $m_1^{(Fe)}$ (dashed line), $m_2^{(Fe)}$ (solid line), $m_3^{(Fe)}$ (dot-dashed line), and the magnitude of the net moment, $|L| = |\underline{m^{(Fe)}} + \underline{m^{(Mn)}}|$ (dotted line), were plotted as a function of time. The $m_2^{(Fe)}$ trace indicates that the sublattice realigned to the $\hat{e}_2$-axis within 3.25 ps, and then oscillated about this new orientation for ~10 ps before stabilizing. During the same time, $m_1^{(Fe)}$ and $m_3^{(Fe)}$ exhibited precessional decay at a lower frequency, proportional to the applied switching anisotropy. The degree of magnetic sublattice misalignment, $|L|$, grew initially during the switching event in a

manner proportional to $\frac{d\underline{m}}{dt}$. This sublattice misalignment was caused by the uniaxial nature of the switching anisotropy, which applied oppositely-pointing torques to the two sublattices. In turn, this drove the sublattices to precess to the new easy axis with opposite chirality, thereby generating a net moment that reached a maximum of 7.3% of $M_s$ at t=3.25 ps (as $m_2^{(Fe)}$ saturated). In the subsequent 10 ps, $L$ oscillated with a periodicity that matched the ringing period observed in $m_2^{(Fe)}$. The similarity between these periods suggests that the system relaxed through the pendulum-like motion of the two sublattices about one another at antiferromagnetic resonance. The Fast Fourier Transform (FFT) of $|L|$ is known to exhibit a peak at twice the antiferromagnetic resonance (AFMR). For the modeled system, this peak occurred at 0.708 THz (shown in the inset of Figure 2(a)), which corresponds with a model-predicted AFMR of 0.354 THz. This simulated resonance is within about 28% of that predicted by theory [41]. The FFT also exhibited some high amplitude, low frequency content, which is attributed to the amplitude decay envelope of $|L|$.

Figure 2(b) shows the results for the voltage-actuated piezoelectric/antiferromagnetic composite model (from Figure 1(b)). In this model, voltage was applied at t=0 ps at the left-most electrode in Figure 1. The values of $\underline{m}^{(\mathrm{Fe})}$ and $|L|$ were plotted together with the volume-averaged biaxial strain state ($\varepsilon_{22} - \varepsilon_{11}$) in the antiferromagnetic disk (on the right ordinate axis). Prior to the application of voltage (i.e., during the magnetic relaxation period, t < 0), magnetoelastic torqueing occurred due to mechanical shear lag effects at the disk edges [8], producing a non-uniform initial sublattice magnetization state with the volume-averaged components $\underline{m}^{(\mathrm{Fe})}$ = (0, 0, 0.78). Then voltage was applied at t=0, and it took 18.5 ps for the voltage-induced strain wave to propagate from the electrode to the edge of the antiferromagnetic disk, as indicated by the first peak in the $\varepsilon_{22} - \varepsilon_{11}$ plot. It took an additional 84 ps (labeled MST in Fig. 2(b)) for the strain to propagate across the disk and cause 90˚ rotation of $\underline{m}^{(\mathrm{Fe})}$. This is seen by the peak of $m_2^{(Fe)}$ concurring with the second peak in $\varepsilon_{22} - \varepsilon_{11}$. Throughout the MST, $m_3^{(Fe)}$ decayed towards zero, as expected, but did not settle completely due to the system's

continued strain oscillations. In contrast, $m_1^{(Fe)}$ remained relatively constant near zero during switching, since the switching occurred primarily in the $\hat{e}_2$-$\hat{e}_3$ plane. With regards to $|L|$, it remained stable around < 2% and, in contrast with the uniform strain model, it did not vary with $\frac{d\underline{m}}{dt}$ in the early part of the MST. These small values of $|L|$ indicate that the voltage-induced switching proceeded below the antiferromagnetic resonance (i.e., near adiabatically [32]), a phenomena also not observed in the uniformly strained model (Figure 2(a)). Subsequent Fourier analysis of $|L|$ indicated broadband low frequency response, which confirms the quasistatic nature of the switching. Further simulations showed that subsequent voltage application to the other top surface electrode in Figure 1(b) resulted in 90˚ in-plane switching from $\hat{e}_2$ to $\hat{e}_1$ with the same frequency response observed during out-of-plane to in-plane switching.

The comparatively slow switching speed of the antiferromagnetic-piezoelectric composite is explained by observing the spin and strain states at two different times, as shown in Figure 3. In Figures 3(a)-(b), for t=71.5 ps and t=102.5 ps respectively, 3-dimensional plots of strain and magnetization are provided from a perspective view (top) and a cross-sectional view (bottom). In Figure 3(a), the strain wave during the MST, indicated by color gradient from red to blue (high strain is red, low strain is blue), had reached the middle the disk. At the same time, the magnetic moments in the strained portion of the disk had rotated in-plane, as shown by red ($\underline{m}^{(\mathrm{Fe})}$) and black ($\underline{m}^{(\mathrm{Mn})}$) arrows, whereas the moments in the unstrained portion of the disk did not move. By the end of the MST, Figure 3(b) shows that the strain had propagated through the entire disk and, correspondingly, the magnetization had rotated uniformly in-plane. Therefore, it is evident that the speed of antiferromagnetic reorientation is dictated by the speed at which strain can propagate through the disk.

While the uniform strain model suggests that near THz switching in an antiferromagnet is possible, the results from the composite model indicate that, for realistic strain-actuated structures, consideration must be given to the method of mechanical actuation. In particular, the two models presented here illustrate 1) that THz switching is possible, 2) that device design choices like the location of the actuating electrode can influence switching speed, and 3) that fully-coupled magnetomechanical models are necessary to predict the frequency response of

strain-controlled antiferromagnets. The results presented here do not mandate that realistic devices be limited to frequencies far below antiferromagnetic resonance. For example, reducing an antiferromagnet's dimension in the direction of mechanical wave propagation should increase operational frequency. Since an antiferromagnet's thickness is commonly its shortest dimension, co-locating the actuating electrode underneath it may increase switching speed up to 20 x.

Furthermore, the energy required to operate at these frequencies can be low. The energy cost per state switch was calculated from the model by numerically integrating the applied charge density over the electrode surface and then using $E_{switch} = QV/2$ to find the energy stored capacitively in the piezoelectric layer. We found that 450 aJ was sufficient to switch axis of antiferromagnetic alignment 90˚. This is 3 orders of magnitude more energy efficient than alternative magnetic control methods, like spin transfer torque, which requires 100 fJ/state switch [33].

In conclusion, a fully-coupled finite element model incorporating micromagnetics, elastodynamics, and piezoelectricity was developed to predict voltage-induced magnetoelastic switching behavior in antiferromagnets. Results demonstrated that the frequency of antiferromagnetic switching can approach THz, but the speed is influenced by the transient of the mechanical excitation. Furthermore, the energy cost associated with controlling antiferromagnetism using strain is extremely low (100's of aJs). This combination of high speed and low power control may offer a new development avenue for next generation devices.

**Acknowledgements**

This material is based upon work supported by, or in part by, the U. S. Army Research Laboratory and the U. S. Army Research Office under contract/grant number W911NF-17-0364. This work was also supported by the NSF Nanosystems Engineering Research Center for Translational Applications of Nanoscale Multiferroic Systems (TANMS) under the Cooperative Agreement Award EEC-1160504.

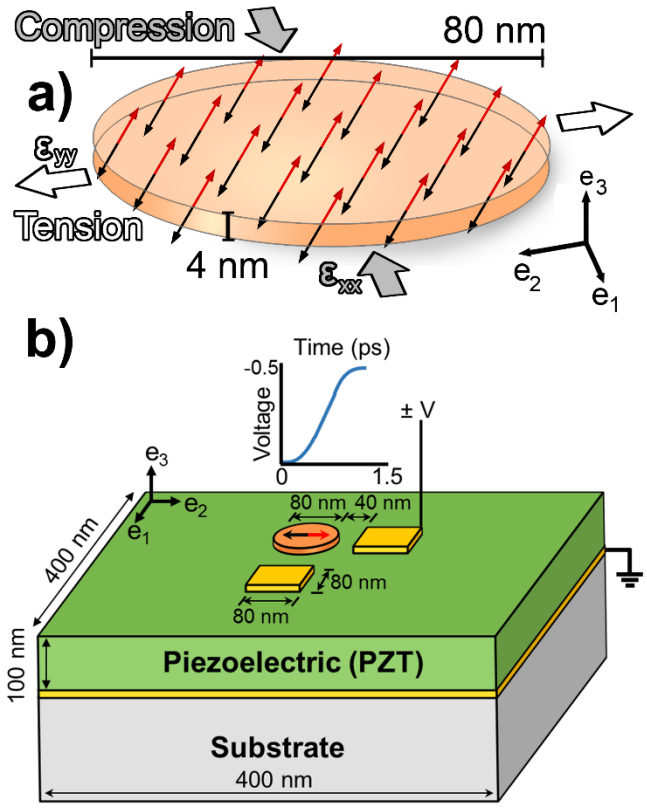


FIG. 1 The geometries used in the finite element calculation are shown. (a) The geometry for the first model is a disk of diameter 80 nm and thickness 4 nm. The antiferromagnetic state is initially aligned out-of-plane and, after magnetically relaxing for 50 ps, remains unmoved. Then, at t=0, the displacement field inside the disk is precisely controlled to yield a uniform biaxial strain of 1400 με, with tension along $\hat{e}_2$ and compression along $\hat{e}_1$. (b) The geometry for the magnetomechanical model of the antiferromagnetic-piezoelectric composite is shown. In this structure, voltages can be applied at either of the two yellow electrodes (with electrical ground on the bottom planar electrode) to generate in-plane strains that can switch the antiferromagnetic state 90˚. The choice of electrode dictates the eventual in-plane direction of the switched antiferromagnet.

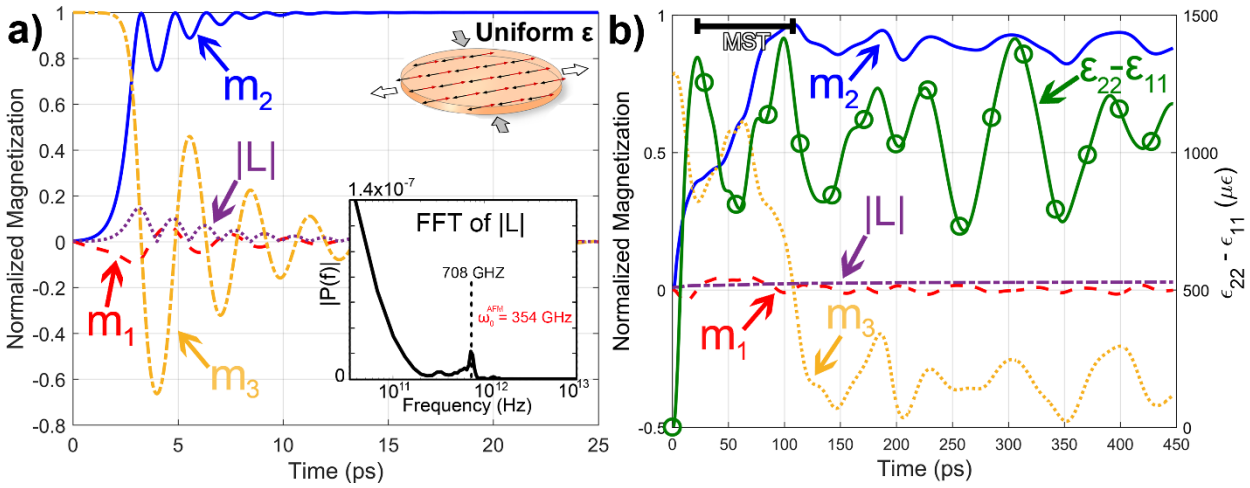


FIG. 2 The volume-averaged magnetization of the Fe sublattice is plotted in time domain for both models. (a) When uniform biaxial strain is instantaneously applied at t=0, the axis of antiferromagnetic alignment resonantly switches within 3.25 ps, and settles about 12 ps later. The peak in the FFT of $|L|$ at 708 GHz corresponds with an antiferromagnetic resonance at half that value, i.e. at 354 GHz (b) When voltage is applied at t=0, antiferromagnetic switching occurs after about 100 ps. The switching process proceeds so far below resonance as to be quasistatic. The observed continuation of motion in $m_2$ is owed to the continuing oscillation in biaxial strain (green line), which occurs because the exciting acoustic wave internally reflects within the antiferromagnetic disk.

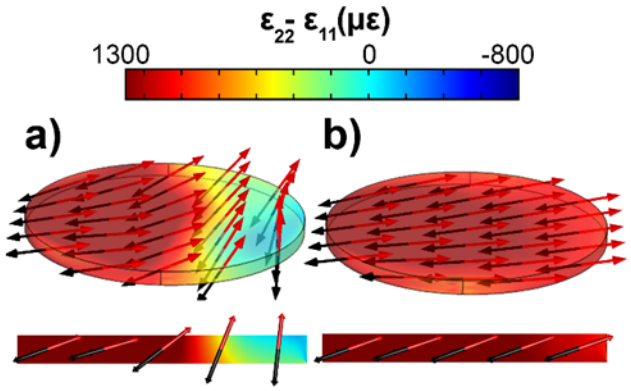


FIG. 3 The strain (3D color plot) and spin states (black and red arrows) of the antiferromagnetic disk in the composite are plotted two different times in the MST. (a) At t=71.5 ps, the wavefront of the acoustic excitation has reached about half way across the disk, and the sublattice moments behind the wavefront have switched in-plane, whereas the moments ahead of the wavefront have not. (b) At t=102.5 ps, the strain has propagated across the disk and switched it completely.

[1] Q. Wang, X. Li, C.Y. Liang, A. Barra, J. Domann, C.S. Lynch, A. Sepulveda, and G.P. Carman, Strain-mediated 180˚ switching in CoFeB and Terfenol-D nanodots with perpendicular magnetic anisotropy, Appl. Phys. Lett. 110, 102903 (2017).

[2] N. D'Souza, M. Salehi Fashami, S. Bandyopadhyay, and J. Atulasimha, Experimental Clocking of Nanomagnets with Strain for Ultralow Power Boolean Logic, Nano Lett. 16, 1069 (2016).

[3] Y. Mukai, H. Hirori, T. Yamamoto, H. Kageyama, and K. Tanaka, Terahertz Nonlinear Magnetic Response in Antiferromagnets, Proc. Conference on Lasers and Electro-Optics 2015, 4 (2015).

[4] H. Kondoh, Antiferromagnetic Resonance in NiO in Far-infrared Region, J. Phys. Soc. Japan 15, 1970 (1960).

[5] L. Alberts and E. W. Lee, Magnetostriction in Antiferromagnetic Nickel Oxide, Proc. Phys. Soc. 78, 728 (1961).

[6] J. P. Domann, W. Y. Sun, L. T. Schelhas, and G. P. Carman, Strain-mediated multiferroic control of spontaneous exchange bias in Ni-NiO heterostructures, J. Appl. Phys. 120, (2016).

[7] A. He, T. Ma, J. Zhang, W. Luo, and M. Yan, Antiferromagnetic $Mn_{50}Fe_{50}$ wire with large magnetostriction, J. Magn. Magn. Mater. 321, 3778 (2009).

[8] C.Y. Liang, S.M. Keller, A.E. Sepulveda, A. Bur, W.Y. Sun, K. Wetzlar, and G.P. Carman, Modeling of magnetoelastic nanostructures with a fully coupled mechanical-micromagnetic model, Nanotechnology 25, 435701 (2014).

[9] J. X. Zhang and L. Q. Chen, Phase-field model for ferromagnetic shape-memory alloys,

Philos. Mag. Lett. 85, 533 (2005).

[10] J. M. Hu, G. Sheng, J. X. Zhang, C. W. Nan, and L. Q. Chen, Phase-field simulation of strain-induced domain switching in magnetic thin films, Appl. Phys. Lett. 98, 88 (2011).

[11] X. Li, D. Carka, C.Y. Liang, A.E. Sepulveda, S.M. Keller, P.K. Amiri, G.P. Carman, and C.S. Lynch, Strain-mediated 180° perpendicular magnetization switching of a single domain multiferroic structure, J. Appl. Phys. 118, 014101 (2015).

[12] C.Y. Liang, S.M. Keller, A.E. Sepulveda, W.Y. Sun, J. Cui, C.S. Lynch, and G.P. Carman, Electrical control of a single magnetoelastic domain structure on a clamped piezoelectric thin film - Analysis, J. Appl. Phys. 116, 0 (2014).

[13] J. Cui, J.L. Hockel, P.K. Nordeen, D.M. Pisani, C.Y. Liang, G.P. Carman and C.S. Lynch, A method to control magnetism in individual strain-mediated magnetoelectric islands, Appl. Phys. Lett. 103, 232905 (2013).

[14] H. Sohn, M.E. Nowakowski, C.Y. Liang, J.L. Hockel, K. Wetzlar, S. Keller, B.M. McLellan, M.A. Marcus, A. Doran, A. Young, and M. Kläui, Electrically driven magnetic domain wall rotation in multiferroic heterostructures to manipulate suspended on-chip magnetic particles, ACS Nano 9, 4814 (2015).

[15] C. Chen, A. Barra, A. Mal, G. Carman, and A. Sepulveda, Voltage induced mechanical/spin wave propagation over long distances, Appl. Phys. Lett. 110, 072401 (2017).

[16] Y. G. Semenov, X. L. Li, and K. W. Kim, Currentless reversal of Néel vector in antiferromagnets, Phys. Rev. B - Condens. Matter Mater. Phys. 95, 1 (2017).

[17] D. Suess, T. Schrefl, W. Scholz, J. V. Kim, R. L. Stamps, and J. Fidler, Micromagnetic simulation of antiferromagnetic/ferromagnetic structures, IEEE Trans. Magn. 38, 2397 (2002).

[18] D. Suess, M. Kirschner, T. Schrefl, J. Fidler, R. L. Stamps, and J.-V. Kim, Exchange bias of polycrystalline antiferromagnets with perfectly compensated interfaces, Phys. Rev. B 67, 54419 (2003).

[19] P. Miltényi, M. Gierlings, J. Keller, B. Beschoten, G. Güntherodt, U. Nowak, and K.D. Usadel, Diluted Antiferromagnets in Exchange Bias: Proof of the Domain State Model, Phys. Rev. Lett. 84, 4224 (2000).

[20] U. Nowak, A. Misra, and K. D. Usadel, Domain State Model for Exchange Bias, J. Appl. Phys. 89, 8 (2000).

[21] G. T. Rado, Mechanism of the magnetoelectric effect in an antiferromagnet, Phys. Rev. Lett. 6, 609 (1961).

[22] G. T. Rado and V. J. Folen, Observation of the Magnetically Induced Magnetoelectric Effect and Evidence for Antiferromagnetic Domains, Phys. Rev. Lett. 7, 310 (1961).

[23] N. Wu, X. He, A.L. Wysocki, U. Lanke, T. Komesu, K.D. Belashchenko, C. Binek, and P.A. Dowben, Imaging and control of surface magnetization domains in a magnetoelectric antiferromagnet, Phys. Rev. Lett. 106, 17 (2011).

[24] F. Máca, J. Mašek, O. Stelmakhovych, X. Martí, H. Reichlová, K. Uhlířová, P. Beran, P. Wadley, V. Novák, and T. Jungwirth, Room-temperature antiferromagnetism in CuMnAs, J. Magn. Magn. Mater. 324, 1606 (2012).

[25] M.J. Grzybowski, P. Wadley, K.W. Edmonds, R. Beardsley, V. Hills, R.P. Campion, B.L. Gallagher, J.S. Chauhan, V. Novak, T. Jungwirth. and F. Maccherozzi, Imaging Current-Induced Switching of Antiferromagnetic Domains in CuMnAs, Phys. Rev. Lett. 118, 1 (2017).

[26] R. C. O'handley, Modern Magnetic Materials: Principles and Applications (2000).

[27] C. Kittel, Theory of Antiferromagnetic Resonance, Phys. Rev. 85, 565 (1952).

[28] A. Vansteenkiste and B. Van De Wiele, MuMax: A new high-performance micromagnetic simulation tool, J. Magn. Magn. Mater. 323, 2585 (2011).

[29] J. Du Shiming Zhou, L. Sun, Exchange Bias Material: FeMn, Handbook of Spintronics, 253 (2016).

[30] T. Ma, J. Zhang, A. He, and M. Yan, Improved magnetostriction in cold-rolled and annealed Mn50Fe50 alloy, Scripta Materialia 61, 427 (2009).

[31] J. T. Lenkkeri, Measurements of elastic moduli of face-centred cubic alloys of transition metals, J. Phys. F Met. Phys. 11, 1991 (1981).

[32] J. Hong, B. Lambson, S. Dhuey, and J. Bokor, Experimental test of Landauers principle in single-bit operations on nanomagnetic memory bits, Sci. Adv. 2, e1501492 (2016).

[33] K. L. Wang, J. G. Alzate, and P. Khalili Amiri, Low-power non-volatile spintronic memory: STT-RAM and beyond, J. Phys. D. Appl. Phys. 46, 74003 (2013).

[34] A. Navabi, C. Chen, A. Barra, M. Yazdani, G. Yu, M. Montazeri, M. Aldosary, J. Li, K. Wong, Q. Hu, and J. Shi, Efficient Excitation of High-Frequency Exchange-Dominated Spin Waves in Periodic Ferromagnetic Structures, Phys. Rev. Applied 7, 034027 (2017).

[35] I. Gilbert, A.C. Chavez, D.T. Pierce, J. Unguris, W.Y. Sun, C.Y. Liang and G.P. Carman, Magnetic microscopy and simulation of strain-mediated control of magnetization in PMN-PT/Ni nanostructures. Appl. Phys. Lett. 109, 162404 (2016).

[36] L. Alberts and E.W. Lee, Magnetostriction in Antiferromagnetic Nickel Oxide. Proceedings of the Physical Society 78, 728 (1961).

[37] P.-d.-V. d. Plessis, S. J. v. Tonder, and L. Alberts, Magnetostriction of a NiO single crystal. II., Journal of Physics C: Solid State Physics 4, 2565 (1971).

[38] T. Yamada, S. Saito, and Y. Shimomura, Magnetic Anisotropy, Magnetostriction, and Magnetic Domain Walls in NiO. II. Experiment., Journal of the Physical Society of Japan 21, 672 (1966).

[39] T. R. McGuire and W.A. Crapo, Magnetic Susceptibility and Magnetostriction of CoO, MnO, and NiO, Journal of Applied Physics 33, 1291 (1962).

[40] T.L. Gilbert, A Phenomenological Theory of Damping in Ferromagnetic Materials, IEEE Transactions on Magnetics 40, 3443 (2004).

[41] J.M.D. Coey, Magnetism and Magnetic Materials, (2010).

[42] D.B. Gopman, J.W. Lau, K.P. Mohanchandra, K. Wetzlar, and G.P. Carman, Determination of the exchange constant of Tb 0.3 Dy 0.7 Fe 2 by broadband ferromagnetic resonance spectroscopy, Phys. Rev. B 93 064425 (2016).

[43] M. Barangi and P. Mazumder, Straintronics-based magnetic tunneling junction: Dynamic and static behavior analysis and material investigation, Appl. Phys. Lett. 104, 162403 (2014).